Time-resolved tomo-PIV measurements to study 3D coherent structures in a pulsed jet in cross-flow.

L. Thomas[1], R. Vernet[1], B. Tremblais[2] and L. David[1]

[1]Institut P', CNRS-ENSMA-Université de Poitiers, Téléport 2, avenue Clément ADER BP 40109, 86961 Futuroscope Chasseneuil

[2]Institut XLIM-SIC, Université de Poitiers, Téléport 2, avenue Clément ADER BP 40109, 86961 Futuroscope Chasseneuil

E-mail: lionel.thomas@univ-poitiers.fr

Abstract: *The recent tomo-PIV technique is presented and apply to a pulsed jet in cross-flow. This technique gives the instantaneous three-dimensional velocity field in a fat sheet (typically the depth of the measurement volume is a tenth of the other dimensions). The results presented here show the applicability of the technique to the characterization of a complex three-dimensional flow.*

Keywords: tomo-PIV, pulsed jet, cross flow, low Reynolds.

1 INTRODUCTION

Natural flows are very complicated and always three-dimensional. Usually, they are studied with punctual measurements to get frequencies or with 2D measurements (via PIV). Tomo-PIV is a recent technique that gives access to the four dimensions of a flow. It has been applied here to evaluate all the potential of the technique to study environmental flows. Some examples of such complicated flows are given by several configurations of discharge of water in a main flow. Pulsed jets in cross-flow are academic flows representative of such more complex configurations.

Jets in cross-flow are highly unsteady and have several distinguishable structures Fric and Roshko (1994). The dominant and distinctive vortical structures associated with the jet in crossflow are: jet shear layer vortices, horseshoe vortices, wake vortices and counter-rotating vortex pair (CVP) which are presented in figure 1. These multiple vortical structures, produced during the jet interaction with

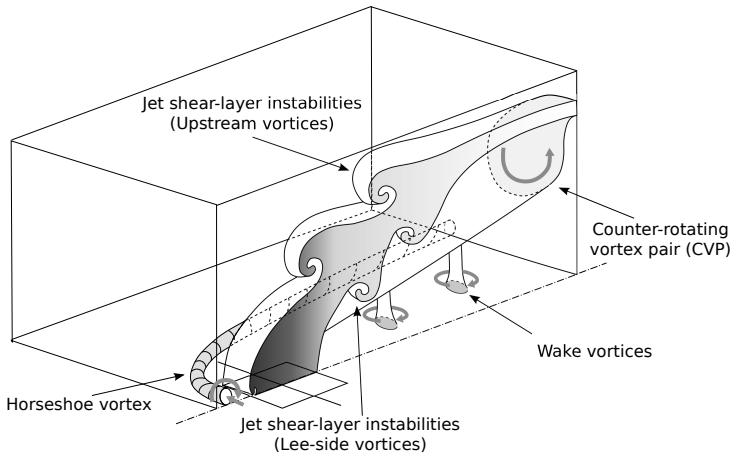

Figure 1: Typical coherent structures in the jet in cross-flow

crossflow, depends on the jet and crossflow parameters ratios, such as velocity ratio, blowing ratio or momentum ratio and the transverse flow regime (laminar or turbulent). These different vortices contribute to obtain better mixing properties compared to the mean flow. Due to the formation of the counter-rotating vortex pair, the transverse flow fluid is entrained under the jet. This entrainment is the main mechanism responsible for the mixing process between the two fluids. Currently, scientists seek to increase the performances of the jet in order to improve its mixing and its penetration in crossflow, by pulsing the jet for instance. Penetration and mixing processes modifications associated with the pulsed jet must be achieved through temporal excitation of the jet flow issuing from the orifice. Effects of pulsing on the jet in crossflow have been studied through the variation of several forcing parameters such as the amplitude (mean and maximum), the signal shape (duty cycle) and the frequency (Johari et al (1999), Eroglu and Breidenthal (2001), Shapiro et al (2006), Gordon et al (2004), M'Closkey et al (2002)).

In the next section of this paper, the experimental setup is presented and the experimental technique used here (tomo-PIV) is detailed, as it is relatively new. Finally, some results are presented.

2 EXPERIMENTAL SETUP

The experimental device is a closed loop horizontal water channel (figure 2). The test section consists of a square duct of 160×160 mm made of altuglass plate. Within the channel, a flat floor is placed to

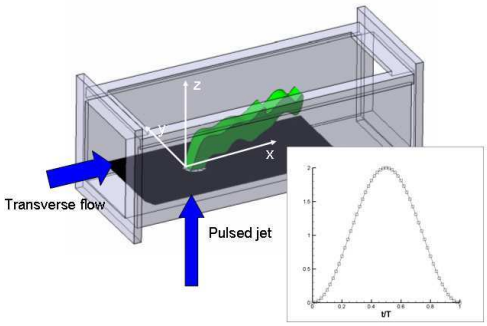

Figure 2: Manipulation scheme for the jet in crossflow

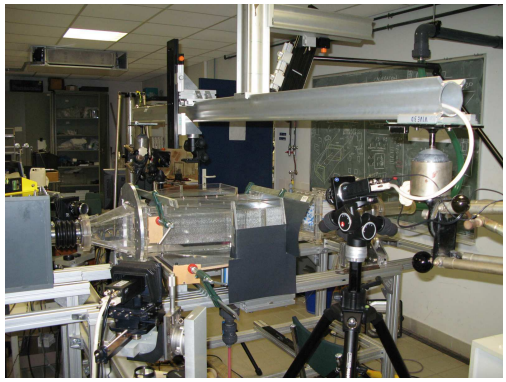

Figure 3: Picture of the experimental setup.

generate a 20 mm thick boundary layer close to the jet nozzle. The square jet of L=30 mm width, flows from bottom to top.
In this study, the jet in crossflow is pulsed with a $1\ Hz$ frequency. The non-dimensional numbers (equation 1) of the flow are the jet-to-crossflow ratio R between the mean jet velocity $\overline{U}_j$ and the crossflow velocity U_{cf} ($R = 1$) and the Reynolds number Re_j based on the mean jet velocity ($Re_j = 500$), the characteristic length L (defined as the length of the square orifice) and the viscosity ν:

$$Re_j = \frac{\overline{U}_j L}{\nu} \qquad R = \frac{\overline{U}_j}{U_{cf}} \tag{1}$$

The pulsed jet injection is characterized by the shape of the signal (sinusoidal), the Strouhal number $St = \frac{fL}{\overline{U}_j}$, the amplitude ratio $A_j = \frac{\Delta U_j}{\overline{U}_j}$. The pulsed jet is generated by two pumps: the first pump produces a steady flow and at the same time, a sinusoidal signal is applied to a second pump in order to obtain a flow rate variation from zero to twice the mean flow rate. In our case, $A_j = 2$ and the $St = 1.8$. Some other usual parameters depend on these two parameters: the ratio of pulse width $\alpha = A_j^{-1}$ and the stroke ratio $S_r = St^{-1}$. The table 1 shows the parameters values used in our experiments.

$f\ (Hz)$	Re_j	R	A_j	α	St	S_r
1	500	1	2	0.5	1.8	0.56

Table 1: Forcing parameters used in our experiments

3 TOMO-PIV

3.1 Overview

The tomo-PIV experimental technique has been used to measure the 3D velocity fields inside a volume. The figure 3 shows the experimental setup with the measurement apparatus. On the photo, the four cameras used around the channel and the laser coming from the top can be observed. Some prisms are added on the channel walls to prevent images from astigmatism.
The tomo-PIV technique is used to measure the 3d velocity field inside a $154 \times 93 \times 25\ mm^3$ volume. The principle is an extension of the classical PIV. Instead of using a thin laser sheet, a fat sheet (typically $1\ cm$ thick) is illuminating the measurement volume, seeded with small particles. Several (typically four) cameras are used in order to reconstruct the light intensity distribution inside a $867 \times 524 \times 143$ volume. This step is detailed in 3.2. This is the more crucial step. Then two subsequent volumes are cross-correlated using interrogation volumes instead of interrogation windows. In our experiment, $48 \times 48 \times 32$ voxels interrogation volumes with 75% overlap are used to get $65 \times 36 \times 10$ vectors.

This technique has been used for the first time by Elsinga et al (2006). It has been improved by several research teams during the last years and is still under heavy development. Atkinson and Soria (2009) modified slightly the original algorithm in order to accelerate the computation. Wieneke (2008) developed a self-calibration procedure. Novara et al (2010) introduced a precision improvement of the method by combining the reconstruction procedure and the displacement estimation. A parametric study has been performed by Thomas et al (2010) in order to optimize the geometric reconstruction parameters. It has been applied for exemple by Scarano and Poelma (2009) in the cylinder wake and by Schroder et al (2008).

3.2 Reconstruction procedure

The reconstruction procedure is an inverse ill-posed problem. The direct problem consists in projecting the volume on images, while the inverse problem consists in reconstructing the volume from the images. The problem is now rather classical in medical applications, but there, the volume is fixed and it is possible to get as many images as needed to get a good reconstruction. The reconstruction procedure is an inversion of the radon transform and it is performed in general in the Fourier domain. Anyway, in fluid mechanics, the number of cameras is limited by the optical access and the cameras high cost. It is known that the limited number of view leads to more noisy reconstruction. In this case, algebraic methods are more adapted (see for example Herman and Lent (1976)), because they introduce some a priori in the computation. The usual algorithm is the MART algorithm which maximizes the entropy.

To apply this algorithm, a calibration procedure is necessary to establish a geometric correspondance between images pixels and volume voxels. Several images of a grid are taken for several in-depth displacements (like in stereo-PIV). Then, a correspondance is established between the grid points real coordinates $\mathbf{X} = (X,\, Y,\, Z)$ and the projection coordinates $\mathbf{x}_n = (x_n,\, y_n)$ on the image n. Here, Z is the coordinate perpendicular to the laser sheet. The volume is enlightened between Z_{min} and Z_{max}. The function ψ_n such as $\mathbf{x}_n = \psi_n(\mathbf{X})$ is modeled for each camera by a pinhole model (or a Soloff polynomial model). It is evaluated using a nonlinear least-squares minimization algorithm. The inverse transformation is also defined for a given Z: $\mathbf{X}_n = (X_n, Y_n) = \psi^{-1}(\mathbf{x}_n,\, Z)$. The set of points in the volume corresponding to the same point is called the line of sight. The intensity I of a point $\mathbf{x}_n$ in image n is given by equation 2.

$$I(\mathbf{x}_n) = \int_{Z_{min}}^{Z_{max}} E(\psi^{-1}(\mathbf{x}_m,\, Z),\, Z) \sqrt{1 + \left|\left| \frac{\partial \psi^{-1}(\mathbf{x}_n,\, Z)}{dZ}(Z) \right|\right|^2}\, dZ \tag{2}$$

where $E(\mathbf{X})$ is the volume intensity at $\mathbf{X}$. As the inversion of the problem is better using algebraic methods, the problem must be discretized. The images are already discretized in pixels indexed by p, defined using the characteristic function χ_p such as $\chi_p(\mathbf{x}_n) = 1$ if $\mathbf{x}_n \in \mathcal{P}(p)$ (where $\mathcal{P}(p)$ is the pixel indexed by p) and 0 otherwise. The volume is discretized in the same way using a basis of functions which are generally also charateristics functions, but which can be also more complicated. It is possible to write $E(\mathbf{X}) = \sum_v E_v \chi_v(\mathbf{X})$. E_v is the total energy of the voxel indexed by v, and the volume $\delta\mathcal{V}_v$ of the voxel indexed by v is defined by $\delta\mathcal{V}_v = \int \chi_v(\mathbf{X})\, d\mathbf{X}$.

It is possible to rewrite the problem with equation 3.

$$I_p = \sum_v w_{pv} E_v \tag{3}$$

where I_p is the total energy received by the pixel indexed by p and w_{pv} is given by equation 4.

$$w_{pv} = \frac{1}{\delta\mathcal{V}_v} \int_{\chi_p(\mathbf{x}_n)=1} \left(\int_{Z_{min}}^{Z_{max}} \chi_v(\psi^{-1}(\mathbf{x}_m,\, Z),\, Z)) \sqrt{1 + \left\| \frac{\partial \psi^{-1}(\mathbf{x}_n,\, Z)}{dZ}(Z) \right\|^2}\, dZ \right) dx_m dy_m \tag{4}$$

w_{pv} has no units and its value is between 0 and 1. It is called the interaction between pixel indexed by p and voxel indexed by v. Its expression is very ugly and difficult to evaluate. For pinhole camera models and characteristic function volume discretization basis, it corresponds to compute the intersection between a cube and a pyramid. Usually, it is approximated. One of the simple way to perform this is to consider that the camera is far enough from the volume, that the size of the projection of the voxel is of the same order as the pixel size, and that the voxel is a cube orientated such as its faces are all parallel or perpendicular to the pixel sides. If the projection of the voxel center on the image n is $(\delta x_n,\, \delta y_n)$ in the pixel coordinate system and δp is the pixel size, then w_{pv} is given by a bilinear interpolation: $w_{pv} = (1 - \frac{\delta x}{\delta p})(1 - \frac{\delta y}{\delta p})$. This approximation has been validated on artificial cases (see Thomas et al (2010)) by comparison with an evaluation of the integral by numerical integration. This approximation is used in the following.

The choice of the discretization scale is important. It is quite logical to take voxels whom projection has a size comparable to a pixel size. It has been shown again by Thomas et al (2010) that around this ratio 1 on 1, there is a possibility to change slightly this ratio without loosing accuracy.

There are several well known iterative algorithm used to solve equation 3. The most commonly used are the MART algorithm and the MLOS-SMART ones. MART is given by equation 5.
For each pixel indexed by p, then for each voxel indexed by v:

$$E_v^{n+1} = E_v^n \left(\frac{I_p}{\sum_u w_{pu} E_u^k} \right)^{\mu w_{pv}} \tag{5}$$

where μ is a relaxation parameter that can be chosen between 0 and 1. This algorithm can be initialized with a uniform value, but it can also be initialized with a minimum line-of-sight first guess. The value of the energy of a given voxel is given by the minimum pixel energy of the main corresponding pixels of each image. (The main corresponding pixel is the pixel inside which the voxel center is projected). This enables to reduce the computation time of the MART iterations if the seeding concentration is low enough. The MLOS-SMART algorithm is similar. The volume is first initialized with a multiplicative line-of-sight first guess (see Atkinson and Soria (2009)). The voxels are then updated iteratively following equation 6. For each voxel indexed by v:

$$E_v^{n+1} = E_v^n \prod_{p/w_{pv}>0} \left[\left(\frac{I_p}{\sum_u w_{pu} E_u^k} \right)^{\mu w_{pv}} \right]^{1/Card\{p/w_{pv}>0\}} \tag{6}$$

The number of iterations is between 3 and 5 for MART, and between 10 and 20 for MLOS-SMART. The computation time is much lower for MLOS-SMART, but the advantage decreases while the seeding concentration increases. Our code is written in C++ using the SLIP library (Tremblais et al (2010)). It uses a MinLOS-MART algorithm based on a minimum line-of-sight first guess and a usual MART algorithm.

3.3 Limitations

The interest of the method are obvious: it is possible to get fully instantaneous 3D velocity measurements. It is interesting even for statistics because velocity gradients are reachable. Anyway, there are several limitations to the technique.

The calibration must be precise, otherwise the lines-of-sight seeing a same particle do not intersect. This problem has been considerably reduced by the development by Wieneke (2008) of the self-calibration algorithm.

There is a compromise to find between seeding density and reconstruction quality. For very low density, the reconstruction is very accurate because no particles are hidden by others. An example of such an ideal reconstruction is given in figure 4. But then, it is only possible to perform tracking on the particles. When the seeding concentration is increased, some “ghost” particles are appearing: an example is given in figure 5. Even if their intensity is often lower, they can have an incidence on the cross-correlation, in particular by smoothing the gradients (see Elsinga et al (2010)). This effect can be reduced by taking into account the fact that very often, the displacement of these “ghost” particles is incoherent (see Novara et al (2010) and Atkinson et al (2010)).

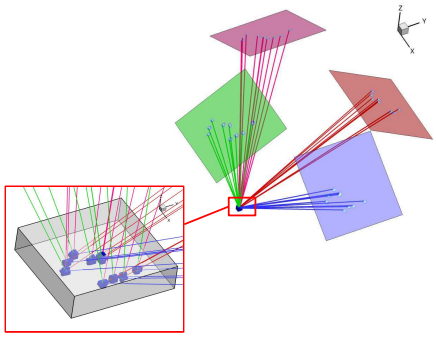

Figure 4: Example of reconstruction with low seeding concentration. The four images are visible. The volume is zoomed on the left. The 10 particles are clearly identified.

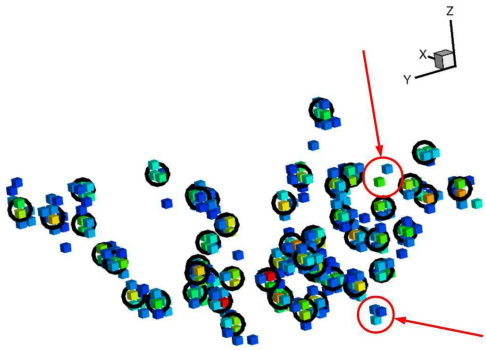

Figure 5: Example of reconstruction with the presence of ghost particles (circled in red). The black circles represent the 50 original particles, put in the same volume as figure 4. The intensity is thresholded in order to see the most intense voxels.

Another difficulty in tomo-PIV is the computation time which is very high, depending on the seeding concentration. It can take up to 8 hours to get one velocity field with a simple MART algorithm with 4 1600$\times$1200 cameras. These problems have been reduced using parallelization.

4 RESULTS

222 velocity fields have been reconstructed. The statistics are presented in figure 6. The most important thing to observe on the mean velocity field is that the injection of fluid is effective only on half of the jet length. There is a competition between the main flow and the injection, as the velocities are of the same order. The dissipation takes place essentially behind the jet, where the Lee-side vortices are moving, but also near the boundary layer, where the horseshoe vortex reconnection takes place. The fluid is then going upwards, entrained by the jet counter-rotating vortex pair. Some instantaneous velocity fields are presented in figure 7. Iso-surfaces of Q-criterion colored by the vorticity vector orientation color code, velocity vectors and velocity fluctuation iso-contours in 3 slices are shown at 8 successive times separated by $1.2\ s$. The temporal evolution is physically realistic. The coherent structures are

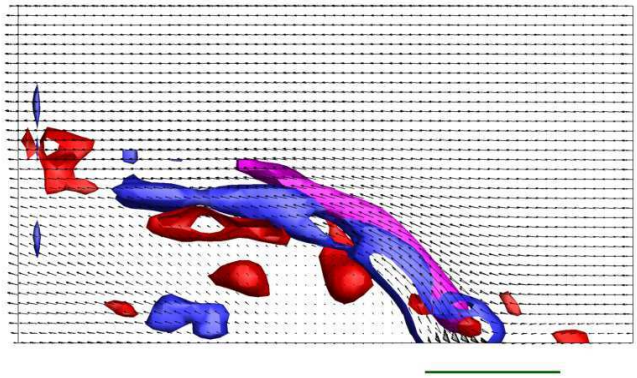

Figure 6: Mean velocity field and iso-surfaces of mean velocity norm (orange), mean dissipation (cyan) and mean Q-criterion (red).

mainly rotating around Z (red and blue). They are convected very slowly with the main flow, with a frequency close to the jet natural frequency (around $0.28\ Hz$), which is different from the forcing frequency ($1\ Hz$). That means that the unstability regime of the jet is absolute in these conditions. The natural unstability is dominating the flow. The forcing doesn't have effects far from the injection. Strong non-linear interactions transfer energy from the forcing towards the global instability.

Moreover, some coherent structures are present in the boundary layer and their dynamics should be explored more in details. In this case, the spatial resolution is too low to look at them carefully.

To consider more closely the effect of forcing, a zoom on the injection is presented in figure 8. ω_z iso-surfaces (red $\omega_z > 0$ – blue $\omega_z < 0$, velocity vectors and velocity fluctuation iso-contours in 3 slices separated by $0.8\ s$ are shown. One vortex is formed upstream the jet (in red) at the forcing frequency and a shear layer is more or less always present downstream the jet (in blue). The upstream vortex disappears periodically, but from the images, it is not clear where it goes. Another important point to notice is that the injection profile is far from being flat. For numerical modeling, this have to be taken into account.

5 CONCLUSION

The recent Tomo-PIV technique has been presented in details. Some measurements have been performed in jet in cross-flow. A brief study of the coherent structures shows the interest of the measurement technique for the study of the instantaneous flow dynamics. The main drawback for the moment is the intensive computation time needed to get the velocity fields and our lack of habit to visualize and analyze the instantaneous three-dimensional flows.

References

Atkinson C, Soria J (2009) An efficient simultaneous reconstruction technique for tomographic particle image velocimetry. Exp in Fluids 47:553–568

Atkinson C, Buchmann N, Stanislas M, Soria J (2010) Adaptative mlos-smart imporved accuracy tomographic piv. In: Proc. 15th Int Symp on Applications of Laser Techniques to Fluid Mechanics, Lisbon, Portugal

Elsinga G, Scarano F, Wieneke B, van Oudheusden B (2006) Tomographic particle image velocimetry. Exp in Fluids 41:933–947

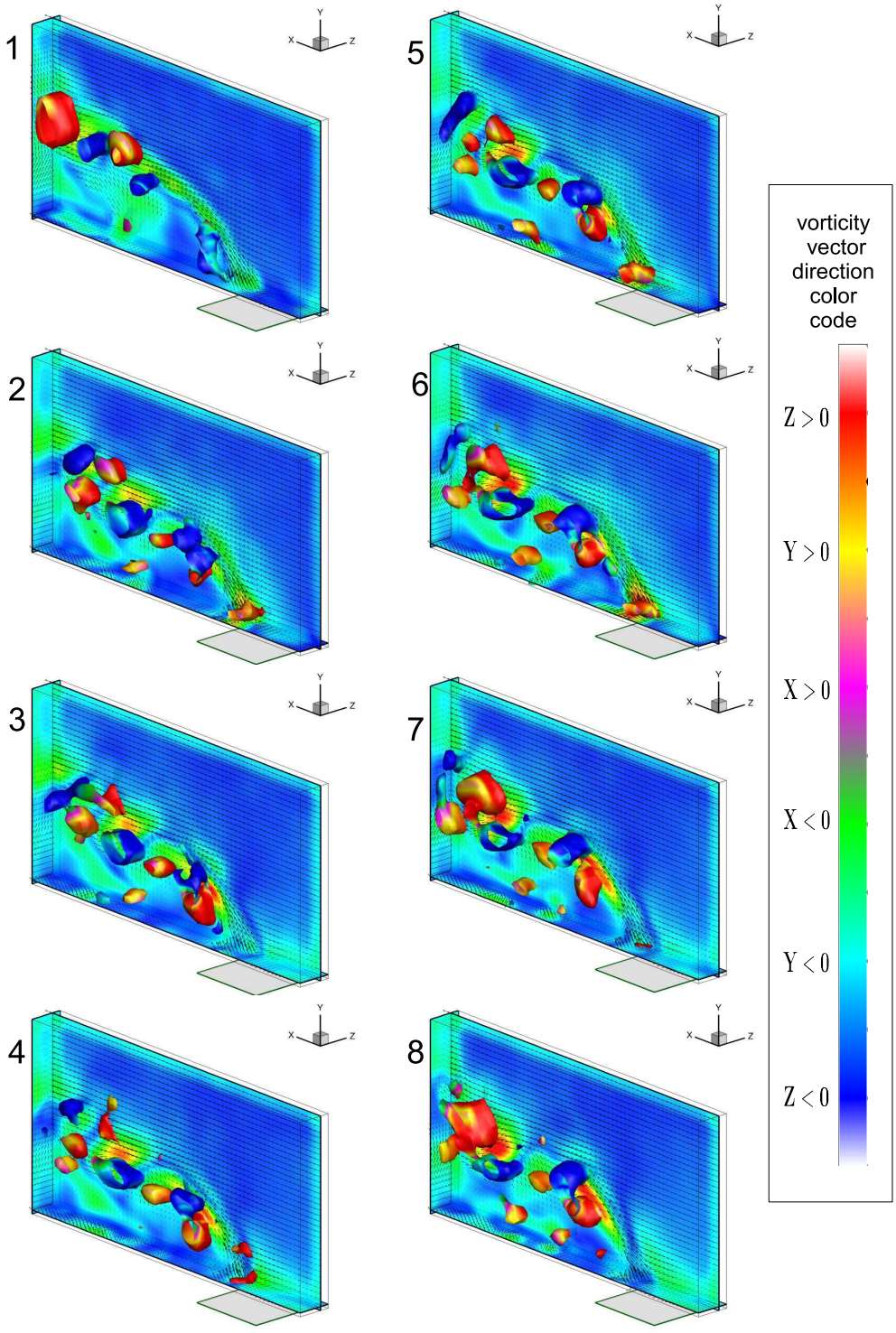

Figure 7: iso-surfaces of Q-criterion colored by the vorticity vector orientation color code, velocity vectors and velocity fluctuation iso-contours in 3 slices at 8 successive times separated by $1.2\ s$.

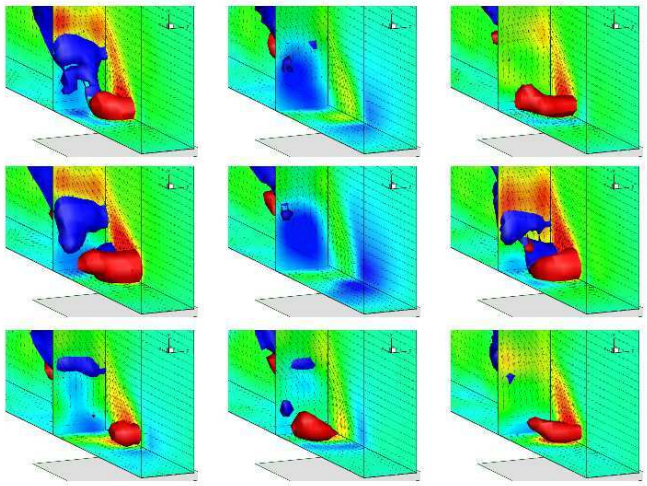

Figure 8: ω_z iso-surfaces (red $\omega_z > 0$ – blue $\omega_z < 0$, velocity vectors and velocity fluctuation iso-contours in 3 slices at 9 times separated by $0.8\ s$.

Elsinga G, Westerweel J, Scarano F, Novara M (2010) On the velocity of ghost particles and the bias errors in tomographic-piv. Exp in Fluids online first:1–14

Eroglu A, Breidenthal RE (2001) Structure, penetration and mixing of pulsed jets in crossflow. AIAA Journal 12(12):1666–1671

Fric T, Roshko A (1994) Vortical structure in the wake of a transverse jet. J Fluid Mech 279:1–47

Gordon M, Cater JE, Soria J (2004) Investigation of the mean passive scalar field in zero-net-mass-flux jets in cross-flow using planar-laser-induced fluorescence. Phys Fluids 16(3):794–808

Herman G, Lent A (1976) Iterative reconstruction algorithms. Comput Biol Med 6:273–294

Johari H, Pacheco-Tougas M, Hermanson JC (1999) Penetration and mixing of fully modulated turbulent jets in crossflow. AIAA Journal 37(7):842–850

M'Closkey RT, King JM, Cortelezzi L, Karagozian AR (2002) The actively controlled jet in crossflow. J Fluid Mech 452:325–335

Novara M, Batenburg K, Scarano F (2010) Motion tracking-enhanced mart for tomographic piv. Meas Sci Technol 21:035,401

Scarano F, Poelma C (2009) Three-dimensional velocity patterns of cylinder wakes. Exp in Fluids 47:69–83

Schroder A, Geisler G, Scarano F, Dierksheide U (2008) Investigation of a turbulent spot and a tripped turbulent boundary layer flow using time-resolved tomographic piv. Exp in Fluids 44:305–316

Shapiro SR, King JM, M'Closkey RT, Karagozian AR (2006) Optimization of controlled jets in crossflow. AIAA Journal 44(6):1292–1298

Thomas L, Vernet R, Tremblais B, David L (2010) Influence of geometric parameters and image pre-processing on tomo-piv results. In: Proc. 15th Int Symp on Applications of Laser Techniques to Fluid Mechanics, Lisbon, Portugal

Tremblais B, David L, Arrivault D, Dombre J, Chatellier L, Thomas L (2010) Slip : Simple library for image processing (version 1.0). http://www.sic.sp2mi.univ-poitiers.fr/slip/, URL http://www.sic.sp2mi.univ-poitiers.fr/slip/

Wieneke B (2008) Volume self-calibration for 3d particle image velocimetry. Exp in Fluids 45(4):549–556